Present Status of Rare-earth Free Ferrimagnet Mn 4 N and Future Prospects of Mn 4 N-based Compensated Ferrimagnets

Takashi Suemasu, Laurent Vila, Jean-Philippe Attané

Present status of rare-earth free ferrimagnet Mn_4N and future prospects of Mn_4N-based compensated ferrimagnets

Takashi Suemasu[1], Laurent Vila[2], Jean-Philippe Attané[2]

[1]*Department of Applied Physics, Faculty of Pure and Applied Sciences, University of Tsukuba, Tsukuba, Ibaraki 305-8573, Japan*
[2]*Université Grenoble Alpes, CEA, CNRS, Spintec, 38054 Grenoble, France*

(Received January 5, 2021)

The rare-earth-free ferrimagnet Mn_4N has attractive features for spintronics applications, because it possesses a perpendicular magnetization, due to a relatively large magnetic anisotropy constant of ~10^5 J m^{-3} and a small spontaneous magnetization of ~100 kA m^{-1}, and a large spin polarization (P = 0.8). More crucially, it is possible to reach the magnetic compensation at room temperature, by tuning its constituent element in compounds such as $Mn_{4-x}Ni_xN$ and $Mn_{4-x}Co_xN$. This is particularly interesting for spin-torque-based spintronics applications, because at the vicinity of the magnetization and/or angular momentum compensation points, the switching currents can be reduced significantly, thereby leading to lower switching energies and higher switching speed. In this review article, we emphasize the importance of epitaxial growth of Mn_4N films by comparing the results obtained on two different substrates, MgO(001) and $SrTiO_3$(001). We then present the achievement of ultrafast current-induced domain wall motion (CIDWM) in Mn_4N microstrips, and study the magnetic compensations in $Mn_{4-x}Ni_xN$ and $Mn_{4-x}Co_xN$ at room temperature, proved by x-ray magnetic circular dichroism measurements. Finally, we offer future prospects for such Mn_4N-based compensated ferrimagnets.

1. Introduction

The ability of spin-transfer torques (STTs) and spin-orbit torques (SOTs) to induce magnetization precession and switching is the basis of a whole range of existing or emerging spintronics technologies.[1)] In this context, ferrimagnets (FIM) have attracted an increasing attention.[2-15)] Their key feature is that their spontaneous magnetizations are much smaller than those of ferromagnets, because the magnetic moments of different sublattices are aligned antiparallel to each other. This parameter is an important asset to develop applications based on STTs and SOTs, in which a flux of angular momentum carried by an incoming spin polarized current acts on the magnetization, inducing magnetization precession and/or switching. In the case of STTs, the spin polarized current is generated within a magnetic layer by the exchange interaction. In the case of SOTs, a pure spin current (i.e., a flow of angular momentum without net charge current) can be generated by spin Hall effect, frequently within a heavy metal layer in contact with the magnetic layer. It can also be produced by the Rashba Edelstein effect, at interfaces breaking the inversion symmetry, or in topological insulators. In all cases, the torque is due to the conservation of angular momentum. When the ferrimagnet is at the vicinity of the magnetic compensation (MC) (and/or angular momentum compensation), the incoming flow of angular momentum affects easily the reduced magnetization, and thus the critical current density necessary for magnetization switching decreases.[5,7,16)]. Ferrimagnets are thus appealing materials to develop STTs and SOTs–based devices such as domain wall memories, skyrmion-motion-based devices, three terminal magnetic random-access memories, SOT oscillators,[17)] and others.[18,19)] The most common route used in spintronics to achieve MC is based on alloys combining rare-earth elements and transition metals such as $Gd_{0.44}Co_{0.56}$ and $Tb_{0.21}Co_{0.79}$.[3,5,6,12,13)] When the magnetization of the two species aligns antiparallel, there exists a single concentration at which the compensation occurs at room temperature (RT). Here, we have paid special attention to rare-earth free ferrimagnets as they alleviate the need of critical elements for spintronics. In Mn_4N, MC can be reached at RT just by tuning its constituent element in $Mn_{4-x}Ni_xN$ and $Mn_{4-x}Co_xN$ films.[20-23)]

Anti-perovskite Mn_4N is ferrimagnetic, and has a Curie temperature of 740 K in bulk Mn_4N,[24)], while Fe_4N, Co_4N, $Fe_{4-x}Co_xN$, and $Fe_{4-x}Ni_xN$ samples possessing the same structure are ferromagnetic[25-30)] at RT. On the other hand, Ni_4N is paramagnetic at RT.[30,31)]~~, except for Ni_4N.[30)]~~ As shown in Fig. 1, there are two inequivalent Mn sites: those at the corner sites, Mn(I), and the others at the face-centered sites, Mn(II). N atoms are positioned at the body-centered

sites. Neutron diffraction in bulk Mn_4N revealed that the magnetic moment of Mn(I) is 3.5 μ_B, while that of Mn(II) is −0.8 μ_B at 300 K,[32] where μ_B is the Bohr magneton. Thus, the magnetic moments of the Mn(I) atoms determine the direction of magnetization. The electron state of Mn_4N has been studied extensively.[33-35] According to an electron diffraction study using 50-nm-thick polycrystalline Mn_4N films, the N atom in Mn_4N was found to behave as an electron acceptor, and the electron state of Mn_4N was expressed as $Mn^0(Mn^{+0.2})_3N^{-0.6}$.[34] This is different from the donor model applicable to ferromagnetic Fe_4N, wherein one electron is donated from the N atom to each of the three face-centered Fe atoms.[36]

The interest of this material for spintronics arises from several features.

i) The combination of a relatively large perpendicular magnetic anisotropy (PMA) with a small Ms leads to perpendicular magnetization, i.e., to the appearance of an out-of-plane easy axis of magnetization. This perpendicular magnetization allows downscaling spintronic devices, and storing data permanently using a bistable magnetization state in STT and SOT-based applications. In this context, Mn_4N thin films are interesting candidates as they have been reported to have a relatively small spontaneous magnetization M_S ~100 kA/m.[32,42,45], with an anisotropy field value $\mu_0 H_K$ > 2.5 T.[40,54] Perpendicular magnetic anisotropy (PMA) has been reported in Mn_4N films deposited on various substrates, including glass, Si(001), MgO(001), $SrTiO_3$[STO](001), $(LaAlO_3)_{0.3}(Sr_2TaAlO_6)_{0.7}$[LSAT](001), and $LaAlO_3$(001),[37-44] and the in-plane tensile strain has been proposed to be the origin of PMA.[40,44] An interesting point is that Mn_4N films are under tensile stress even when grown on LSAT(001), which has a smaller lattice constant than Mn_4N, corresponding to a lattice mismatch of 0.8%[43] which might be considered to induce compressive stress in Mn_4N layers. The uniaxial magnetic anisotropy constant (K_u) of Mn_4N thin films has been reported to be of the order of 10^5 J/m^3.[42,45-47]. A theoretical study has been recently conducted on the contribution of N to the in-plane tensile strain and to the resultant PMA in Mn_4N.[48] Materials such as Mn_4N, where the PMA is large enough to overcome the demagnetizing field energy, are perpendicularly magnetized.

ii) The effective spin polarization extracted from DW velocity measurements in

Mn_4N[16] is relatively high (P=0.8). This allows enhancing the magnetotransport effects used in spintronics such as the Anomalous Hall Effect, the Giant magnetoresistance, and suggests for instance that Mn_4N could be used as a magnetic soft layer in a Magnetic Tunnel Junction stack.

iii) The magnetization reversal occurs through nucleation and the motion of Bloch domain walls (DWs). The combination of a relatively large spin polarization with a small Ms leads to high domain wall velocities due to the STT.[16] The current-induced velocity due to the adiabatic torque is indeed given by

$$v \approx \frac{1}{1+\alpha^2}\frac{g\mu_B}{2eM_S}PJ \propto \frac{P}{M_S} \qquad (1)$$

where v is the DW velocity, α the damping constant, g the Landé factor, e the electron charge, μ_B the Bohr magneton, P the current spin polarization and J the current density. Note that the interest of the small magnetization is not restricted to the case of pure STT on domain walls: for both STT through magnetic tunnel junction and for SOTs, the torque efficiency is supposed to vary as the inverse of the free layer magnetization.

iv) The combination of a high PMA with a reasonable exchange constant leads to relatively sharp Bloch walls. Sharp DWs could lead to an enhanced spin transfer effect through the non-adiabatic contribution[49] and contribute to faster DW motion at smaller currents.[47] The width of the DW (Δ) in the nanowire is given by Eq. (2):[50]

$$\Delta = \sqrt{A/K_u} \qquad (2)$$

where A is the exchange stiffness. As K_u increases, Δ decreases, leading to the reduction in the threshold current density (j_{th}) necessary to move the DWs.[47,51] In this respect, materials with PMA are advantageous for current-induced domain wall motion (CIDWM) devices. Furthermore, the DW width needs to be small enough to scale DW-based logic devices,[52] and three terminal or racetrack memories[53] down to the ultimate technology nodes.

v) Mn_4N does not require chemical elements deemed as critical from geopolitical and environmental points of view, such as heavy metals and rare-earth.

In this review article, we begin by underlining the importance of a high-quality thin-film

growth on the magnetic properties, by comparing the epitaxial growth of Mn_4N films on STO(001) and MgO(001) substrates.

2. Formation and characterizations of Mn_4N films on STO(001) and MgO(001)

10-nm-thick Mn_4N layers were grown on MgO(001) and STO(001) substrates at 450 °C, using a molecular beam epitaxy system with an ion-pump (10^{-7} Pa), equipped with a high temperature Knudsen cell for Mn and a radio-frequency (RF) N_2 plasma.[40,54] To prevent oxidation, the samples were capped with 3-nm-thick SiO_2 layers. In the case of STO(001) substrates, we used a buffered NH_4F-HF solution with controlled pH values to obtain TiO_2 atomic plane-terminated surfaces, with steps one unit cell in height.[55] The crystalline quality of the Mn_4N layers was characterized by 20-kV reflection high-energy electron diffraction (RHEED), and X-ray diffraction (XRD) with a Cu Kα radiation source. Magneto-transport properties, such as the magnon-magnetoresistance (MMR)[56,57] and the anomalous Hall effect (AHE), were measured by the Van der Pauw method for Mn_4N blanket layers at RT.[58] The transverse voltage (V_y) can be expressed as Eq. (1): [59]

$$V_y = \left(R_{\mathrm{H}} \frac{B_Z}{t} + \frac{\rho_{\mathrm{AHE}}}{t} \right) I_x = \frac{\rho_{\mathrm{xy}}}{t} I_x, \qquad (1)$$

where R_{H}, B_Z, t, ρ_{AHE}, I_x, and ρ_{xy} are the normal Hall coefficient, the magnetic flux density perpendicular to the sample surface, the film thickness, the anomalous Hall resistivity, the longitudinal current, and the Hall resistivity, respectively.

Figures 2(a) and 2(b) show out-of-plane XRD profiles of Mn_4N epitaxial films on MgO(001) and STO(001) substrates, respectively.[58] Figures 2(c) and 2(d) are their in-plane XRD profiles when the scattering vector was set to be along [100]. In both samples, oriented diffraction peaks such as 002 and 004 together with RHEED streaks are the proof of the epitaxial growth of Mn_4N films. Superlattice diffractions from N atoms positioned at the body-centered site, marked by arrows, are also present. However, there is a big difference in crystalline quality between them. ω-scan rocking curves are shown in the same figure for (e) Mn_4N 002 and (f) Mn_4N 004. We used the higher-order Mn_4N 004 for Mn_4N films on STO because the peak position of Mn_4N 002 is close to STO 002 in Fig. 2(b). According to the fitting by a Lorentzian function, the full-width at half maximum was 2.5 and 0.14 deg. for Mn_4N films on MgO and STO, respectively. The lattice constant of MgO is 0.421 nm, and that of STO is 0.391 nm. Thereby, the lattice mismatch for Mn_4N/MgO(001) and Mn_4N/STO(001)

is approximately −7.6% and −0.4%, respectively, assuming that the Mn_4N films has a cubic structure and a lattice constant of 0.389 nm.[32] Such a small lattice mismatch between Mn_4N and STO leads to the perfect epitaxial growth of Mn_4N/STO[16] as shown in Fig. 2(g), whereas misfit dislocations are observed for Mn_4N/MgO[41] in Fig. 2(h).

Figures 3(a) and 3(b) show the dependence of the longitudinal resistance R_{xx} with the magnetic field normal to the sample surface. The resistivity ρ_{xx} is 187 μΩ cm for the Mn_4N/MgO sample, and 181 μΩ cm for the Mn_4N/STO sample at RT. As shown in these figures, the magnetoresistance is dominated by the magnon magnetoresistance, typically observed in samples with a strong uniaxial anisotropy.[60] Figures 3(c) and 3(d) show the hysteresis loops measured by AHE. The AHE angle ρ_{xy}/ρ_{xx} is high (−2%), in line with previous reports on Mn_4N.[61,62] The coercivity of the Mn_4N/STO sample (0.26 T) is slightly smaller than that of the Mn_4N/MgO sample (0.44 T). These relatively high coercive fields are due to the small saturation magnetization. The Mn_4N/MgO sample shows a smooth hysteresis loop. In contrast, the magnetization of the Mn_4N/STO sample switches very sharply, with a full remanence at zero field. Despite these differences, it is striking that the spontaneous magnetization and all the transport quantities of the two systems are very similar. This result indicates that the Mn_4N films in the two samples are intrinsically alike, regardless of the different substrates and thus of different lattice mismatches. The increased disorder in the Mn_4N films on MgO widens the nucleation and DW pinning field distribution associated to the defects, thus leading to a higher coercivity and a slanted hysteresis loop. Figures 3(e) and 3(f) present the hysteresis loops for in-plane and out-of-plane fields, obtained by VSM-SQUID up to 4 and 6 T, respectively. From the out-of-plane hysteresis curves, the M_S of Mn_4N/MgO and Mn_4N/STO samples was found to be 118 and 105 kA m^{-1}, respectively. From the in-plane loop of Mn_4N/STO, the anisotropy field $\mu_0 H_K$ was estimated to be 4 T. The uniaxial anisotropy K_u was calculated to be 1.1×10^5 J m^{-3}, using the integration of the area enclosed between the in-plane and out-of-plane magnetization curves, and taking into account the demagnetization energy. Now we can discuss the magnetic domain configuration in Mn_4N thin films. The theoretical equilibrium domain size in Mn_4N layers is determined by the balance between the dipolar energy and the DW energy. From the measured values of M_S = 105 kA m^{-1}, K_u = 110 kJ m^{-3}, and A = 15pJ m^{-1} (using a rough estimation from the Curie temperature),[63] the DW width can be calculated to be $\Delta = \sqrt{A/K_u} = 11\ nm$. The resulting equilibrium domain size for a

10-nm-thick Mn_4N film, calculated using the analytical model of Ref. 64, is of several km. This indicates that the demagnetizing field is negligible because of the small M_S, and that in practice the domain size and shape are rather determined by DW pinning on extrinsic defects.[65] Hereafter, we focus on Mn_4N epitaxial films on STO(001).

Let us examine the domain pattern in Mn_4N layers on STO substrates. The magnetic domain configuration was observed by magneto-optical Kerr effect (MOKE) microscopy. The observation was performed both for the as-deposited state in Fig. 4(a) and for a partially reversed state in Fig. 4(b), corresponding to the red dot state in the magnetization curve shown in Fig. 4(c). In Fig. 4(a), the magnetic domain size d_p is as large as 20 μm, with smooth magnetic DWs. This value is comparable with the equilibrium value of ultrathin CoFeB (1.1 nm)/MgO(1) and Pt(2.4)/Co(0.27) system, with d_p values of respectively 14 and 6.5 μm obtained after thermal demagnetization.[66,67] Figure 4(b) presents the domain configurations in partially reversed states. The domain size in Mn_4N/STO reaches a value as large as one millimeter. MOKE images show the presence of very few nucleation centers, showing that the magnetization switching occurs by nucleation, followed by an easy propagation of DWs. This observation is consistent with the fact that the hysteresis loop is square. Note that the use of MgO substrate leads to much smaller sub-micrometric domains, which is consistent with the observation of a larger disorder using structural and magnetic characterizations [ref. 58]. On the basis of these results, we can state that the selection of a well-matching substrate is crucial to improve the magnetic properties of Mn_4N layers, and notably its suitability for current-induced DW propagation.

3. Evaluation of DW speed and spin transfer efficiency

10-nm-thick Mn_4N epitaxial films were processed by ion milling into sets of twenty 1 or 2 μm wide microstrips, connected to two electric pads. The current flows through the microstrips in order to induce DW motion. After saturation of the magnetization, magnetic field pulses were applied to nucleate a domain in a pad and to inject DWs into the microstrips. The DWs were then pushed by current pulses. The DW displacement during the current pulses was measured using a differential MOKE imaging technique, consisting in subtracting the MOKE image before pulse injection from the image obtained after the pulse injection, to highlight the difference between them and showing the corresponding magnetization reversal by DW displacement. Figure 5(a) shows the differential MOKE image after domain nucleation using a

field pulse of 0.6 T for 300 μs, and Fig. 5(b) shows the differential MOKE image taken after injection of several 1 ns current pulses. The area through which the DW propagated appears in black. The DW motion direction is opposite to the current, and thus follows the electrons flow. Figure 5(c) presents the current density dependence of the DW velocity v_{DW}. The threshold current density for 1-ns-width pulse is 3.0×10^{11} A m^{-2}. Above 8×10^{11} Am^{-2} in 1-μm-wide strips, the trend of the v_{DW} versus j curve becomes linear. In the studied range of current densities, the DW reached an average velocity of 900 m s^{-1}, for a current density of 1.3×10^{12} A m^{-2} in both 1-μm and 2-μm-wide strips. This value is the highest in all materials and structures whose DW was driven by only pure STTs. The velocities observed in Mn_4N can thus be considered as a milestone in the history of STTs.

The large v_{DW} obtained in Mn_4N show that the STTs can be competitive with SOTs even though SOTs-driven DW dynamics have been the focus of nearly the entire community in recent years. SOTs have been found to be an efficient mechanism to drive DWs in non-centrosymmetric multilayers, in which a FM is deposited on a heavy metal like Pt.[68,69] The prototypical example is AlO_x/Co(0.6nm)/Pt,[70] where the chiral Néel structure acquired by the DWs in the presence of interfacial Dzyaloshinskii-Moriya interaction[71] leads to a high mobility (v_{DW} = 400 m s^{-1} for $j = 3 \times 10^{12}$ A m^{-2}). Higher SOT-driven v_{DW}'s were obtained recently in a multilayer structure in which two Co/Ni layers were coupled anti-ferromagnetically through a Ru layer,[72] or in GdCo ferrimagnet layers deposited on top of Pt.[73] In these systems the v_{DW} was clearly observed to vary with the total magnetization. In the former experiment, a maximum velocity of v_{DW} = 750 m s^{-1} for $j = 3 \times 10^{12}$ A m^{-2} was obtained at RT using a Ru spacer layer. Thus, the stack magnetization was reduced to 8% of the M_S of a single Co/Ni layer. In the latter one, a peak velocity of 1300 m s^{-1} was reported at the compensation temperature, for $j = 2 \times 10^{12}$ A m^{-2} and still high even at 300 K with 850 m s^{-1}. Recently, SOT driven DW motion in insulating ferrimagnetic garnets have also led to similar DW speeds.[74] In this context, the v_{DW} presented here at RT for DWs in Mn_4N is comparable to the best results obtained using SOTs. Moreover, this constitute the first demonstration of very efficient current-driven DW motion by pure STT using a system with PMA. Another figure of merit of the STT efficiency is the DW mobility $\eta = \Delta v_{DW}/\Delta j$, that can be derived from the v_{DW} versus j curve, and is equal to $\eta = 7.1 \times 10^{-10}$ m^{3}C^{-1}. This mobility is also the highest value in all STT-driven systems, and is superior to most SOT-driven records. Above 1.3×10^{12} A m^{-2}, many domains nucleate, probably because the sample reaches 745K, the Curie temperature of Mn_4N, and becomes

temporarily paramagnetic.

4. Formation and characterizations of 3d-doped compensated Mn_4N films

On the basis of the DW experiments presented above, much faster v_{DW} can therefore be expected in the vicinity of the angular momentum compensation point, which is supposed to be close to the MC point in 3d-element-doped Mn_4N. In the past, Mekata et al. attempted to replace some of the Mn atoms in Mn_4N by In and Sn, and obtained the MC with appropriate composition ratios and temperature.[75] Here we present our recent results obtained on $Mn_{4-x}Ni_xN$ and $Mn_{4-x}Co_xN$ epitaxial films grown on STO(001). Preparation details are given in Refs. 21 and 23. We performed x-ray absorption spectroscopy (XAS) and x-ray magnetic circular dichroism (XMCD) measurements at the twin APPLE-II undulator beam line BL16A of KEK in Japan, to find a Ni ratio in $Mn_{4-x}Ni_xN$ and a Co ratio in $Mn_{4-x}Co_xN$ where the MC occurs at RT. These techniques are quite powerful to determine element-specific electronic structures. Among samples, $Mn_{4-x}Co_xN$ (x = 0.8) was measured at the twin helical undulator beamline BL23SU of SPring-8 in Japan, wherein the measurements were performed using the total electron yield (TEY) mode both at the Mn $L_{2,3}$ and Co $L_{2,3}$ absorption edges.[76] All measurements were performed at RT. We also measured the AHE loops at RT for a magnetic field applied perpendicularly to the plane, using the Van der Pauw method.

4.1 Mn substitution by Ni

Approximately 30-nm-thick $Mn_{4-x}Ni_xN$ (x = 0, 0.1, 0.25, and 0.5) thin films were grown on STO(001) substrates at 450 °C by MBE. The deposition rates of Mn and Ni were measured, and independently controlled by changing the crucible temperature of each Knudsen cell. An approximately 3-nm-thick SiO_2 capping layer was used for AHE measurements, while Ti capping layers were used for XAS and XMCD measurements. Figure 6 shows the out-of-plane XRD and RHEED patterns of the $Mn_{4-x}Ni_xN$ (x = 0, 0.1, 0.25, and 0.5) thin films along the STO[100] azimuth. Diffraction peaks of the grown layers appear at small 2θ angles in Fig. 6 and overlap with the intense diffraction peaks of the STO substrate because of the excellent lattice match between the $Mn_{4-x}Ni_xN$ films and the STO(001) substrate. Very sharp, streaky lines together with superlattice lines marked by arrows appeared in the RHEED patterns, and Kikuchi lines also verified the highly *c*-axis-oriented epitaxial growth of the $Mn_{4-x}Ni_xN$ films. Notably, the diffraction peaks of $Mn_{4-x}Ni_xN$ appear at slightly higher angles

than those of cubic STO(001) in Fig. 6, showing the ratio of perpendicular lattice constant *c* to in-plane lattice constant *a*, *c*/*a*, is smaller than 1. This result indicates the presence of in-plane tensile strain in the $Mn_{4-x}Ni_xN$ films at $x \leq 0.5$.

Figure 7 shows the AHE loops for $Mn_{4-x}Ni_xN$ (x = 0, 0.1, 0.25, and 0.5) thin films at RT. It is noted that the sign of ρ_{xy} was reversed for $Mn_{4-x}Ni_xN$ films between x = 0.1 and 0.25 in Fig. 7, indicating the crossing of the magnetic compensation point. Such a sign reversal is commonly used to confirm the presence of a MC point in rare-earth ferrimagnets.[4,5] The ratio of the remnant magnetization (M_r) to M_S, M_r/M_S, was almost 1 for x = 0, 0.1, and 0.25. In contrast, $Mn_{3.5}Ni_{0.5}N$ films showed a much smoother magnetization reversal, and saturating their magnetization required a large magnetic field. The reasons for this behavior could be the degradation of the crystalline quality at x = 0.5 and the decrease of the magnetization, which can both contribute to an increase of the coercivity. We therefore chose the samples x = 0.1 and 0.25, and performed XAS and XMCD measurements.

Figures 8(a) and 8(b) show the XAS (blue) and XMCD (black) spectra of $Mn_{3.9}Ni_{0.1}N$ and $Mn_{3.75}Ni_{0.25}N$ films at the Ni $L_{2,3}$ absorption edges, respectively. Both a magnetic field of ±3 T and circularly polarized x-rays with left or right polarization were applied perpendicularly to the plane. The x-ray polarization was switched at every energy point with a frequency of 10 Hz using five kicker magnets. Spectra at the Mn $L_{2,3}$ absorption edges were acquired in the TEY mode, while those at the $L_{2,3}$ absorption edges in the total fluorescence yield (TFY) mode. This prevents Ni $L_{2,3}$ spectra from overlapping with background signals. Regarding the XAS spectra of $Mn_{3.9}Ni_{0.1}N$ and $Mn_{3.75}Ni_{0.25}N$ films, only the sharp main peaks are observed at the L_3 edge (852–853 eV) and the L_2 edge (870 eV). Similar peaks were reported for $NiFe_3N$.[77] In contrast, we see shoulders in the XAS spectrum of Ni-rich Ni_3FeN films,[77] wherein Ni atoms unavoidably occupy face-centered II sites. These shoulders are observed approximately 2 eV above the Ni $L_{2,3}$ main peaks. Such shoulders are reported for other antiperovskite ferromagnetic nitrides such as Fe_4N and Co_4N films above the Fe (Co) $L_{2,3}$ main peaks.[78,79] They are interpreted to originate from the electric dipole transition from the metal 2*p* core level to the hybrid state between the orbitals of the N 2*p* and metal 3*d* at II sites, indicating that the objective element is at the face-centered sites in Fig. 1.[78] From these results, we can safely state that Ni atoms preferentially occupy the I sites in Mn_4N when $x \leq 0.25$. Regarding the peak sign of the XMCD spectra, they are opposite at the $L_{2,3}$ edges between $Mn_{3.9}Ni_{0.1}N$ and $Mn_{3.75}Ni_{0.25}N$. Thus, the directions of the magnetic moments of Ni(I) in $Mn_{3.9}Ni_{0.1}N$ films are

different from that in $Mn_{3.75}Ni_{0.25}N$ films with respect to magnetizations.

We next discuss the XAS (blue) and XMCD (black) spectra of $Mn_{3.9}Ni_{0.1}N$ and $Mn_{3.75}Ni_{0.25}N$ films at the Mn $L_{2,3}$ absorption edges in Figs. 8(c) and 8(d). Here we focus on the XMCD spectra. In Fig. 8(c), in $Mn_{3.9}Ni_{0.1}N$ the signs of the XMCD signals around the Mn L_3 edge are positive, negative, and positive from low to high photon energy. The superposition of spectra with different signs indicates that the magnetic moments of Mn(I) and Mn(II) are aligned antiparallel to each other. In our previous studies on Fe_4N films, the transition metals at the I(II) site exhibited localized (itinerant) states, which is supported by first-principles calculation using the all-electron full-potential linearized augmented-plane-wave (FLAPW) method and Fermi's golden rule with E1 transitions.[78] Similar results are also observed for Mn_4N using FLAPW calculation.[76] Therefore, the XMCD spectra of $Mn_{3.9}Ni_{0.1}N$ and $Mn_{3.75}Ni_{0.25}N$ films can also be viewed as an overlap of such localized and itinerant components characterized by features α and β, respectively, with opposite signs. In $Mn_{3.9}Ni_{0.1}N$, the broad positive peak (β) near 642 eV likely originates from Mn(II) atoms, caused by the hybridization between Mn(II) 3*d* and N 2*p* orbitals. In contrast, the sharp negative peak (α) near 640 eV likely comes from Mn(I), which is remote from the body-centered N atom, and therefore entails less hybridization. On the other hand, the signs of the XMCD signals near the Mn L_3 absorption edges in Fig. 8(d) are negative, positive, and negative from low to high photon energy in $Mn_{3.75}Ni_{0.25}N$, which is the opposite to the results obtained for the $Mn_{3.9}Ni_{0.1}N$ films. We attribute this to magnetization reversal at both the I and II sites of Mn atoms. Such behavior of the spectra was reported in ferrimagnets at the vicinity of the compensation temperature.[80,81] It is also notable that the XMCD signal at the Ni L_3 absorption edge has the opposite sign of the sharp peak (α) for the Mn L_3 edge at 640 eV regardless of *x*, and has the same sign as that of the broad spectrum (β) at 642 eV. Thus, the magnetic moments of Ni(I) align in parallel with those of Mn(II) in the studied range of Ni content *x*. From these discussions, we conclude that the Ni atoms preferentially occupy the I site in $Mn_{4-x}Ni_xN$ thin films, and that the magnetic moments of Ni atoms are parallel to those of Mn(II). The simplified schematics of the magnetic structures in $Mn_{4-x}Ni_xN$ below the MC composition ratio in Fig. 8(e) and above it in Fig. 8(f). Therefore, we can safely state that the MC occurs at a certain value *x* between 0.1 and 0.25 at RT.

4.2 Mn substitution by Co

30-nm-thick $Mn_{4-x}Co_xN$ (x = 0 – 1.3) thin films were grown on STO(001) substrates at approximately 450 °C by MBE. The deposition rates of Mn and Co were independently measured and controlled by changing the crucible temperature of each Knudsen cell. An approximately 3-nm-thick SiO_2 capping layer was used for AHE measurements, while Ta capping layers were employed for XAS and XMCD measurements. Both a magnetic field of ±5 T and circularly polarized X-rays with left or right polarization were applied at an angle of 54.7° to the plane.[82] The X-ray polarization was switched at every energy point with a frequency of 10 Hz using five kicker magnets. The energy of the incident soft X-rays was adjusted to include the L_2 and L_3 absorption edges of Mn and Co. The XAS spectra were obtained in TEY mode and TFY mode at the Mn $L_{2,3}$ and Co $L_{2,3}$ absorption edges, respectively.

Figure 9 shows the out-of-plane XRD profiles and RHEED patterns of the $Mn_{4-x}Co_xN$ thin films along the STO[100] azimuth. *c*-axis-oriented XRD peaks such as 001, 002, and 004 of $Mn_{4-x}Co_xN$ appeared at slightly higher angles compared to those of STO. For samples with x = 0–1.1, the diffraction peaks of $Mn_{4-x}Co_xN$ 002 and 004 with RHEED streaks confirm the epitaxial growth of $Mn_{4-x}Co_xN$ films. Superlattice diffractions from N atoms at the body-centered site are also present for samples with x = 0–0.8, as indicated by the white arrows. With increasing x, however, the XRD peak intensity decreased, the RHEED streaks were blurred at x = 1.2, and the diffraction peak of 004 was not observed at x = 1.1 and 1.2, meaning that the crystalline quality degraded. The in-plane lattice constant a decreased from 0.389 nm (x = 0) to 0.384 nm (x = 1.3). The out-of-plane lattice constant c also decreased from 0.386 nm to 0.381 nm, keeping the in-plane tetragonal distortion (c/a ~ 0.99). Figures 10(a)–10(h) shows the ρ_{AHE} vs. $\mu_0 H$ curves at RT. The magnitude of ρ_{AHE} decreases with x, and its sign reverses between x = 1.1 and 1.2. In the case of $Mn_{4-x}Ni_xN$ films, the sign reverses between x = 0.1 and 0.25 in Fig. 7, which is consistent with the MC composition for this material. We therefore chose the two samples (x = 0.8 and 1.3) together with one more sample (x = 0.2), and performed XAS and XMCD measurements.

Figures 11(a)–11(c) show the XAS and XMCD spectra of $Mn_{4-x}Co_xN$ films (x = 0.2, 0.8, and 1.3) at the Co $L_{2,3}$ absorption edges, and Figs. 11(d)–11(f) show those at the Mn $L_{2,3}$ absorption edges, respectively. Here, we focus on the XMCD spectra. The peaks A and A' in Figs. 11(a) and 11(b) have opposite signs. According to our previous work,[75] Co atoms were found to preferentially occupy I sites, Co(I), when x = 0.8 in $Mn_{4-x}Co_xN$, and the magnetic

moment of Co(I) aligned antiparallel to that of Mn(I). Thus, it is reasonable to state that the Co atoms are positioned at I sites when x = 0.2. Because the signs of the Mn and Co XMCD signals reversed between x = 0.2 in Figs. 11(a, b) and 0.8 in Figs. 11(d, e), respectively, we conclude that all magnetic moments of Mn(I), Mn(II), and Co(I) reverse between these two compositions, and that the MC occurs in the range of $0.2 < x < 0.8$. At present, we do not have sufficient data to discuss the reason why the sign reversal in ρ_{AHE} was absent between x = 0.2 and 0.8 in Fig. 10, and further studies are mandatory on this issue. The XMCD spectrum of Co atoms at x = 1.3 in Fig. 11(c) is more complex than those of the other two compositions. This spectrum can be viewed as an overlap of two sets of components (A–A' and B–B'), which have opposite signs. It is notable that the sign of the peak A(A') at x = 1.3 is opposite to that at x = 0.8, meaning that the magnetic moments of Co(I) atoms reversed between these two compositions. Considering that the Co composition x is 1.3, higher than 1, some of the Co atoms are likely to be positioned at II sites, Co(II). The peak position of B (B') was slightly shifted from that of A(A'), similar to peaks α and β in Figs. 11(d) and 11(e). Thus, we interpret peaks B and B' in Fig. 11(c) to originate from Co(II) atoms with their magnetic moments aligned antiparallel to those of Co(I). We can therefore state that all the magnetic moments of Mn and Co atoms reverse between x = 0.8 and x = 1.3, suggesting that MC occurs in the range of $0.8 < x < 1.3$. This is consistent with the sign reversal of ρ_{AHE} between x = 1.1 and 1.3 in Fig. 10. Figure 11(g) shows simplified schematic illustrations of the magnetic structures in $Mn_{4-x}Co_xN$, based on the above discussions. We used x = 0.2, 0.8, and 1.3 samples in this work; however, the Co compositions are 0.25, 0.75, and 1.25 to simplify the representation in Fig. 11(g). Please note that we do not mean to exclude the possibility that all I sites are occupied with Co atoms when x = 1.3. Our findings show that the MC presumably occurs both between x = 0.2 and 0.8, and between x = 0.8 and 1.3. Observation of a MC at two low temperatures have already been reported[83] and have been studied theoretically.[84] However, to our knowledge there has been no report thus far of the existence of two MC compositions at RT just by doping.

5. Future prospects of Mn_4N-based ferrimagnets

At the vicinity of MC in $Mn_{4-x}Ni_xN$ and $Mn_{4-x}Co_xN$, much faster v_{DW} than those obtained in Mn_4N can be expected, at RT, asthe efficiency of STT in these systems is primarily due to the low magnetization. The combination of SOTs to STTs in these layers, for instance by adding a neighbouring spin Hall effect layer, might be beneficial for inducing DW motion and

magnetization switching. To develop spintronics applications, it would also be worthwhile to check if the relatively high spin polarization of Mn_4N-based ferrimagnets could be used to obtain significant Tunnel Magnetoresistance ratios. Also, the double MC at RT found in $Mn_{4-x}Co_xN$ is very attractive from application perspectives, because the observed double MC mechanism might constitute a route to preserve the MC within a relatively wide range of Co concentrations, providing that one can find compensation concentrations close enough to each other. This is important because several magnetic quantities such as v_{DW} change sharply at the vicinity of the MC, and slight concentration variations may induce undesirable results. From the fundamental viewpoint, it would be interesting to compare the magnetic and spintronic properties such as SOT, STT, AHE, and polarization at the vicinity of the two MC concentrations. It is notable that double MC may occur also in $Mn_{4-x}Ni_xN$ at RT, when Ni atoms start to occupy the face-centered sites with their magnetic moments aligned with Mn(I) atoms when $x > 0.5$. In this context, double MCs are likely to occur in other Mn_4N-based ferrimagnets. As shown in Fig. 5(c), the DW mobility is quite high in Mn_4N, compared to those achieved in SOTs. However, the threshold current density, j_{th}, for DWs to start moving in Mn_4N is relatively high, probably caused by a large damping constant α. It was measured to be around 0.1–0.2 at RT from the linewidth of microwave absorption spectra and the oscillation frequency of time-resolved MOKE signals.[85] This value is much greater than those reported on Fe_4N(α ~ 0.03),[86] and higher by two orders of magnitude than those of MnGa alloys.[87] We are not sure why α is so large for Mn_4N at the moment. Thus extensive studies are mandatory to solve this issue. ~~As j_{th} is proportional to α, we have to consider how to reduce α in Mn_4N-based materials.~~ In any case, the results presented in this article prove the versatility of doped Mn_4N thin films, and open up a rare-earth free platform for ferrimagnetic spintronics.

An unexplored aspect is the use of heavy metal to induced Dzyaloshinskii Moriya interaction (DMI) and to take benefit of SOT altogether with the STT. Thin layers of the Mn_4N family can be covered by a heavy metal in order to induce DMI and generate a transfer of angular momentum to enhance the current induced domain wall motion. It would be interesting to find a material combination where the direction of motion of STT and SOT adds up. If DMI could be large, it would be possible to obtain small skyrmions in thin Mn_4N layers.

Finally, the large tuning of the coercivity observed under a gate application through the STO substrate [ref. 16] is another route to tailor the magnetic state of Mn_4N. This is a very appealing way to achieve a very energy efficient control of its magnetic properties, yet the

origin; strain, charge transfer or ionic migration; has to be elucidated.

6. Conclusion

In this article, we review the potential of rare-earth free Mn_4N for spintronics, from the fundamental properties of Mn_4N such as the excellent epitaxial growth on STO(001) substrates, the AHE loops, and the domain structures observed by MOKE, to the latest results on CIDWM in Mn_4N microstrips, in which v_{DW} reaches 900 m s^{-1}. Mn_4N shows perpendicular magnetic anisotropy, and has a high magnetic anisotropy constant of ~10^5 J m^{-3}, a small spontaneous magnetization of ~100 kA m^{-1} and a large spin polarization as inferred from the large DW velocity. One of the striking features of this material is that magnetic compensation occurs at RT just by tuning its constituent element by doping. The sign reversal of the XMCD signals was observed in $Mn_{4-x}Ni_xN$ and $Mn_{4-x}Co_xN$ epitaxial films between below and above the MC compositions. The two different MC compensations appearing in $Mn_{4-x}Co_xN$ should also exist Mn_4N-based ferrimagnets. To further develop applications based on STTs and/or SOTs, several material properties have to be studied more detailedly, such as the spin current polarization and the damping parameter. Also, using and enhancing spin-orbit effects such as the SOTs or the Dzyaloshinskii Moriya interaction will require depositing ultrathin films of Mn_4N-based ferrimagnets, with a very high quality. These material developments could help confirming the potential of Mn_4N beyond DW manipulation by pure STT, from SOTs[88,89] to skyrmions [7,90] or THz switching.[91,92] We therefore hope that many researchers will be interested in using this material.

Acknowledgment

This work was supported in part by the Japan Society for the Promotion of Science KAKENHI (Grants No. 19K21954, No. 19KK0104, and No. 19K21954). We acknowledge funding from the IDEX of University Grenoble Alpes, through the International Strategic Partnership Project DOMINO, and from the ANR project CONTRABASS. The XMCD experiment was performed at beamline BL-16A of KEK-PF with the approval of the Photon Factory Program Advisory Committee (Proposal No. 2018P011 and No. 2019G574) with the help of Professor K. Amemiya. Special thanks are given to Associate Professor K. Toko, Dr S. Pizzini, Dr J. Vogel, Dr. H. Okuno, Dr. T. Gushi, Dr. K. Ito (Tohoku University at present), Mr. S. Ghosh, Mr. T. Komori, Mr. T. Hirose, Ms. H. Mitarai, and past students of the University of Tsukuba for their

experiments and fruitful discussions.

1) B. Dieny, I.L. Prejbeanu, K. Garello, P. Gambardella, P. Freitas, R. Lehndorff, W. Raberg, U. Ebels, S.O. Demokritov, J. Akerman, A. Deac, P. Pirro, C. Adelmann, A. Anane, A.V. Chumak, A. Hirohata, S. Mangin, S.O. Valenzuela, M. Cengiz Onbaşlı, M. d'Aquino, G. Prenat, G. Finocchio, L. Lopez-Diaz, R. Chantrell, O. Chubykalo-Fesenko and P. Bortolotti, Nat. Electron. **3**, 446 (2020).

2) C. D. Stanciu, A.V. Kimel, F. Hansteen, A. Tsukamoto, A. Itoh, A. Kirilyuk and Th. Rasing, Phys. Rev. B **73**, 220402(R) (2006).

3) C. D. Stanciu, A. Tsukamoto, A. V. Kimel, F, Hansteen, A. Kirilyuk, A. Itoh and Th. Rasing, Phys. Rev. Lett. **99**, 217207 (2007).

4) S. Fukami, T. Suzuki, Y. Nakatani, N. Ishiwata, M. Yamanouchi, S. Ikeda, N. Kasai and H. Ohno, Appl. Phys. Lett. **98**, 082504 (2011).

5) K.-J. Kim, S. K. Won, Y. Hirata, S.-H. Oh, T. Tono, D.-H. Kim, T. Okuno, W. S. Ham, S. Kim, G. Go, Y. Tserkovnyak, A. Tsukamoto, T. Moriyama, K.-J. Lee and T. Ono, Nat. Mater. **16**, 1187 (2017).

6) Y. Hirata, D.-H. Kim, T. Okuno, T. Nishimura, D.-Y. Kim, Y. Futakawa, H. Yoshikawa, A. Tsukamoto, K.-J. Kim, S.-B. Choe and T. Ono, Phys. Rev. Rev. B **97**, 220403(R) (2018).

7) L. Caretta, M. Mann, F. Buttner, K. Ueda, B. Pfau, C. M. Gunther, P. Hessing, A. Churikova, C. Klose, M. Schneider, D. Engel, C. Marcus, D. Bono, K. Bagschik, S. Eisebitt and G. S. D. Beach, Nat. Nanotechnol. **13**, 1154 (2018).

8) S. A. Siddiqui, J. Han, J. T. Finley, C. A. Ross and L. Liu, Phys. Rev. Lett. **121**, 057701 (2018).

9) S.-H. Oh, S. K. Kim, D.-K. Lee, G. Go, K.-J. Kim, T. Ono, Y. Tserkovnyak and K.-J. Lee, Phys. Rev. B **96**, 100407(R) (2017).

10) R. Blasing, T. Ma, S.-H. Yang, C. Garg, F. K. Dejene, A. T. N'Diaye, G. Chen, K. Liu and S. S. P. Parkin, Nat. Commun. **9**, 4984 (2018).

11) S.-H. Yang, K.-S. Ryu and S. Parkin, Nat. Nanotechnol. **10**, 221 (2015).

12) M. Binder, A. Weber, O. Mosendz, G. Woltersdorf, M. Izquierdo, I. Neudecker, J. R. Dahn, T. D. Hatchard, J.-U. Thiele, C. H. Back and M. R. Scheinfein, Phys. Rev. B **74**, 134404 (2006).

13) T. Okuno, K.-J. Kim, T. Tono, S. Kim, T. Moriyama, H. Yoshikawa, A. Tsukamoto and T. Ono, Appl. Phys. Express **9**, 073001 (2016).

14) K. Cai, Z. Zhu, J. M. Lee, R. Mishra, L. Ren, S. D. Pollard, P. He, G. Liang, K. L. Teo and H. Yang, Nat. Electronics **3**, 37 (2020).

15) J. Yu, X. Qiu, Y. Wu, J. Yoon, P. Deorani, J. M. Besbas, A. Manchon and H. Yang, Sci. Rep. **6**,1 (2016).

16) T. Gushi, M. J. Klug, J. P. Garcia, S. Ghosh, J.-P. Attané, H. Okuno, O. Fruchart, J. Vogel, T. Suemasu, S. Pizzini and L. Vila, Nano Lett. **19**, 8716 (2019).

17) Z. Duan, A. Smith, L. Yang, B. Youngblood, J. Lindner, V. E. Demidov, S. O. Demokritov and I. N. Krivorotov, Nat. Commun. **5**, 5616 (2014).

18) J. Finley, C. H. Lee, P. Y. Huang and L. Liu, Adv. Mater. **31**, 1805361 (2019).

19) R. Mishra, J. Yu, X. Qiu, M. Motapothula, T. Venkatesan and H. Yang, Phys. Rev. Lett. **118**, 167201 (2017).

20) T. Komori, T. Gushi, A. Anzai, L. Vila, J.-P. Attané, S. Pizzini, J. Vogel, S. Isogami, K. Toko and T. Suemasu, J. Appl. Phys. **125**, 213902 (2019).

21) T. Komori, T. Hirose, T. Gushi, K. Toko, T. Hanashima, L. Vila, J.-P. Attàne, K. Amemiya and T. Suemasu, J. Appl. Phys. **127**, 043903 (2020).

22) K. Ito, Y. Yasutomi, S. Zhu, M. Murmamat, M. Tahara, K. Toko, R. Akiyama, Y. Takeda, Y. Saitoh, T. Oguchi, A. Kimura and T. Suemasu, Phys. Rev. B **101**, 104401 (2020).

23) H. Mitarai, T. Komori, T. Hirose, K. Ito, S. Ghosh, S. Honda, K. Toko, L. Vila, J.-P. Attané, K. Amemiya and T. Suemasu, Phys. Rev. Mater. **4**, 094401 (2020).

24) C. Li, Y. Yang, L. Lv, H. Huang, Z. Wang and S. Yang, J. Alloys Compd. **457**, 57 (2008).

25) G. Shirane, W.J. Takei, S.L. Ruby, Phys. Rev. **126**, 49 (1962).

26) S. Kokado, N. Fujima, K. Harigaya, H. Shimizu, and A. Sakuma, Phys. Rev. B **73**, 172410 (2006).

27) Y. Komasaki, M. Tsunoda, S. Isogami, and M. Takahashi, J. Appl. Phys. **105**, 07C928 (2009).

28) K. Ito, K. Harada, M. Ye, A. Kimura, Y. Takeda, Y. Saitoh, H. Akinaga, and T. Suemasu, Appl. Phys. Lett. **99**, 252501 (2011).

29) K. Ito, T. Sanai, S. Zhu, Y. Yasutomi, K. Toko, S. Honda, S. Ueda, Y. Takeda, Y. Saitoh, Y. Imai, A. Kimura, and T. Suemasu, Appl. Phys. Lett. **103**, 232403 (2013).

30) F. Takata, K. Ito, S. Higashikozono, T. Gushi, K. Toko, and T. Suemasu, J. Appl. Phys. **120**, 083907 (2016).

~~30) F. Takata, K. Ito, Y. Takeda, Y. Saitoh, K. Takanashi, A. Kimura, and T. Suemasu, Phys. Rev. Mater. **2**, 024407 (2018).~~ → 77)

31) M. Meinert, J. Phys.: Condens. Matter **28**, 056006 (2016).

32) W. J. Takei, R. R. Heikes and G. Shirane. Phys. Rev. **125**, 1893 (1962).

33) K. Kuriyama, S. Hosoya and T. Suzuki, Phys. Rev. **130**, 898 (1963).

34) S. Nagakura and N. Otsuka, J. Phys. Soc. Jpn. **39**, 1047 (1975).

35) S. Matar, P. Mohn, G. Demazeau and B. Siberchicot, J. Phys. France **49**, 1761 (1988).

36) G. W. Wiener and J. A. Berger, J. Metals **7**, 360 (1955).

37) K. M. Ching, W. D. Chang, T. S. Chin, J. G. Duh and H. C. Ku, J. Appl. Phys. **76**, 6582 (1994).

38) K. M. Ching, W. D Chang and T. S. Chin, J. Alloys. Compd. **222**, 184 (1995).

39) M. Tsunoda and K. Kabara, *presented at International Conference of the Asian Union of Magnetics Societies (ICAUMS) 2012*, 2pPS-47, Nara, Japan, 2012.

40) Y. Yasutomi, K. Ito, T. Sanai, K. Toko and T. Suemasu, J. Appl. Phys. **115**, 17A935 (2014).

41) X. Shen, A. Chikamatsu, K. Shigematsu, Y. Hirose, T. Fukumura and T. Hasegawa, Appl. Phys. Lett. **105**, 072410 (2014).

42) K. Kabara and M. Tsunoda, J. Appl. Phys. **117**, 17B512 (2015).

43) T. Hirose, T. Komori, T. Gushi, K. Toko and T. Suemasu, J. Cryst. Growth **535**, 125566 (2020).

44) T. Hirose, T. Komori, T. Gushi, A. Anzai, K. Toko and T. Suemasu, AIP Adv. **10**, 025117 (2020).

45) A. Anzai, F. Takata, T. Gushi, K. Toko and T. Suemasu, J. Cryst. Growth **489**, 20 (2018).

46) T. Komori, A. Anzai, T. Gushi, K. Toko and T. Suemasu, J. Cryst. Growth **507**, 163 (2019).

47) S. Emori and G. S. D. Beach, Appl. Phys. Lett. **98**, 132508 (2011).

48) S. Isogami, K. Masuda and Y. Miura, Phys. Rev. Mater. **4**, 014406 (2020).

49) C. Burrowes, A. P. Mihai, D. Ravelosona, J.-V. Kim, C. Chappert, L. Vila, A. Marty, Y. Samson, F. Garcia-Sanchez, L. D. Buda-Prejbeanu, I. Tudosa, E. E. Fullerton and J.-P. Attàne, *Nat. Phys.* **6**, 17 (2010).

50) A. Thiaville, J. M. García and J. Miltat, J. Magn. Magn. Mater. **242-245**, 1061 (2002).

51) A. Mougin, M. Cormier, J. P. Adam, P. J. Metaxas and J. Ferré, Europhys. Lett. **78**, 57007 (2007).

52) F. Parveen, Z. He, S. Angizi, and D. Fan, *IEEE Computer Society Annual Symposium on VLSI (ISVLSI)* (2017) p.152.

53) S. Fukami and H. Ohno, Jpn. J. Appl. Phys. **56**, 0802A1 (2017).

54) K. Ito, Y. Yasutomi, K. Kabara, T. Gushi, S. Higashikozono, K. Toko, M. Tsunoda and T. Suemasu, AIP Adv. **6**, 056201 (2016).

55) M. Kawasaki, K. Takahashi, T. Maeda, R. Tsuchiya, M. Shinohara, O. Ishiyama, T. Yonezawa, M. Yoshimoto and H. Koinume, Science **266**, 1540 (1994).

56) A. P. Mihai, J. P. Attané, A. Marty, P. Warin, and Y. Samson, Phys. Rev. B **77**, 060401(R) (2008).

57) V. D. Nguyen, L. Vila, P. Laczkowski, A. Marty, T. Faivre, and J. P. Attané, Phys. Rev. Lett. **107**, 136605 (2011).

58) T. Gushi, L. Vila, O. Fruchart, A. Marty, S. Pizzini, J. Vogel, F. Takata, A. Anzai, K. Toko, T. Suemasu, and J.-P. Attané, Jpn. J. Appl. Phys. **57**, 120310 (2018).

59) H. Ohno, A. Shen, F. Matsukura, A. Oiwa, A. Endo, S. Katsumoto, and Y. Iye, Appl. Phys. Lett. **69**, 363 (1996).

60) V. D. Nguyen, L. Vila, P. Laczkowski, A. Marty, T. Faivre, J.-P. Attané, Phys. Rev. Lett. **107,** 136605 (2011).

61) M. Meng, S. X. Wu, L. Z. Ren, W. Q. Zhou, Y. J. Wang, G. L. Wang, and S. W. Li, Appl. Phys. Lett. **106**, 032407 (2015).

62) K. Kabara, M. Tsunoda, and S. Kokado, AIP Adv. **7**, 056416 (2017).

63) K. Ito, N. Rougemaille, S. Pizzini, S. Honda, N. Ota, T. Suemasu, and O. Fruchart, J. Appl. Phys. **121**, 243904 (2017).

64) V. Gehanno, Y. Samson, A. Marty, B. Gilles, and A. Chamberod, J. Magn. Magn. Mater. 172, 26 (1997).

65) J. P. Attané, Y. Samson, A. Marty, J. C. Toussaint, G. Dubois, A. Mougin, and J. P. Jamet, Phys. Rev. Lett. **93**, 257203 (2004).

66) M. Yamanouchi, A. Jander, P. Dhagat, S. Ikeda, F. Matsukura, and H. Ohno, IEEE Magn. Lett. **2**, 3000304 (2011).

67) F. Ando, H. Kakizakai, T. Koyama, K. Yamada, M. Kawaguchi, S. Kim, K.-J. Kim, T. Moriyama, D. Chiba, and T. Ono, Appl. Phys. Lett. **109**, 022401 (2016).

68) S. Emori, U. Bauer, S.-M. Ahn, E. Martinez, and G. S. D. Beach, Nat. Mater. **12**, 611 (2013).

69) K.-S. Ryu, L. Thomas, S.-H. Yang, and S. Parkin, Nat. Nanotechnol., **8**, 527 (2013).
70) I. M. Miron, T. Moore, H. Szambolics, L. D. Buda-Prejbeanu, S. Auffret, B. Rodmacq, S. Pizzini, J. Vogel, M. Bonfim, A. Schuhl, and G. Gaudin, nature mater. **10**, 419 (2011).
71) A. Thiaville, S. Rohart, É. Jué, V. Cros, and A. Fert, Europhys. Lett. **100**, 57002 (2012).
72) S.-H. Yang, K.-S. Ryu, and S. Parkin, Nat. Nanotechnol. **10**, 221 (2015).
73) L. Caretta, M. Mann, F. Büttner, K. Ueda, B. Pfau, C. M. Günther, P. Hessing, A. Churikova, C. Klose, M. Schneider, D. Engel, C. Marcus, D. Bono, K. Bagschik, S. Eisebitt, and G. S. D. Beach, Nat. Nanotech. **13**, 1154 (2018).
74) C. O. Avci, E. Rosenberg, L. Caretta, F. Büttner, M. Mann, C. Marcus, D. Bono, C. A. Ross and G. S. D. Beach, Nat. Nanotechnol. **14**, 561 (2019).
75) M. Mekata, J. Phys. Soc. Jpn. **17**, 5 (1962).
76) K. Ito, Y. Yasutomi, S. Zhu, M. Nurmamat, M. Tahara, Y. Takeda, Y. Saitoh, K. Toko, R. Akiyama, T. Oguchi, A. Kimura, and T. Suemasu, Phys. Rev. B **101**, 104401 (2020).
77) F. Takata, K. Ito, Y. Takeda, Y. Saitoh, K. Takanashi, A. Kimura, and T. Suemasu, Phys. Rev. Mater. **2**, 024407 (2018).
78) K. Ito, K. Toko, Y. Takeda, Y. Saitoh, T. Oguchi, T. Suemasu, and A. Kimura, J. Appl. Phys. **117**, 193906 (2015).
79) K. Ito, T. Sanai, Y. Yasutomi, S. Zhu, K. Toko, Y. Takeda, Y. Saitoh, A. Kimura, T. Suemasu, J. Appl. Phys. 115, 11C712 (2014).
80) E. Goering, S. Gold, and G. Schütz, J. Synchrotron Rad. **8**, 422 (2001).
81) H. Maruyama, and N. Nakamura, J. Electron Spectrosc. Relat. Phenom. **136**, 135 (2004).
82) J. Stöhr, and H. König. Phys. Rev. Lett. **75**, 3748 (1995).
83) S. Ohkoshi, T. Hozumi, M. Utsunomiya, M. Abe, and K. Hashimoto, Physica B **329–333**, 691 (2003).
84) Y. F. Zhang and S. L. Yan, Solid State Commun. **146**, 478 (2008).
85) S. Isogami, A. Anzai, T. Gushi, T. Komori, Y. K. Takahashi, and T. Suemasu, JSAP Spring Meeting 10a-M101-7, Tokyo, March 10, 2019.
86) S. Isogami, M. Tsunoda, M. Oogane, A. Sakuma, and M. Takahashi, J. Magn. Soc. Jpn. **38**, 162 (2014).
87) S. Mizukami, F. Wu, A. Sakuma, J. Walowski, D. Watanabe, T. Kubota, X. Zhang, H. Naganuma, M. Oogane, and Y. Ando, Phys. Rev. Lett. **106**, 117201 (2011).
88) K. Cai, Z. Zhu, J. M. Lee, R. Mishra, L. Ren, S. D. Pollard, P. He, G. Liang, K. L. Teo and

H. Yang, Nat. Electron. **3**, 37 (2020).
89) K. Ueda, M. Mann, P. W. P. de Brouwer, D. Bono and G. S. D. Beach, Phys. Rev. B **96**, 064410 (2017).
90) Y. Hirata, D. H. Kim, S. K. Kim, D. K. Lee, S. H. Oh, T. Nishimura, T. Okuno, Y. Futakawa, H. Yoshikawa, A. Tsukamoot, Y. Tserkovnyak, Y. Shiota, T. Moriyama, S. B. Choe, K. J. Lee and T. Ono, Nat. Nanotechnol **14**, 232 (2019).
91) S. Mangin, M. Gottwald, C-H. Lambert, D. Steil, V. Uhlíř, L. Pang, M. Hehn, S. Alebrand, M. Cinchetti, G. Malinowski, Y. Fainman, M. Aeschlimann and E. E. Fullerton, Nat. Mater. 13, 286 (2014).
92) S. Wienholdt, D. Hinzke and U. Nowak, Phys. Rev. Lett. **108**, 247207 (2012).

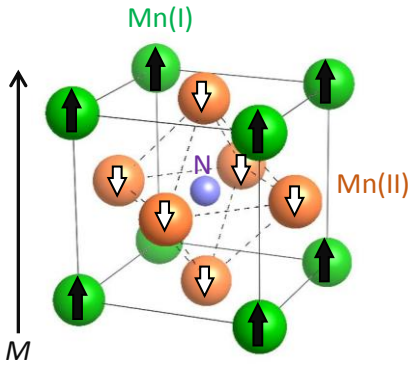

Fig. 1 Crystal structure of anti-perovskite-type Mn_4N. The magnetic moment of the corner-site Mn atoms, Mn(I), is antiparallel to that of the face-centered Mn atoms, Mn(II), and parallel to the overall magnetization (black arrow).

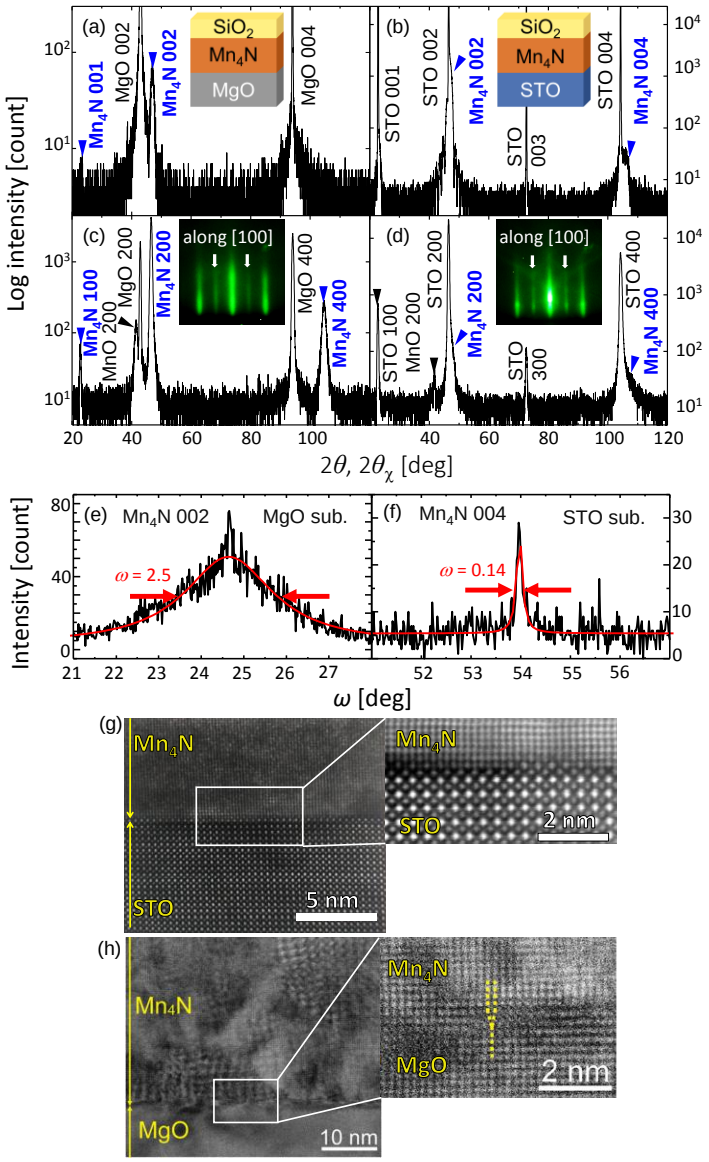

Fig. 2 XRD profiles of Mn_4N films on (a, c, e) MgO(001) and (b, d, f) STO(001) substrates. (a, b) Out-of-plane XRD patterns. The insets show the stack structures. Copyright 2018 Japan Society of Applied Physics. (c, d) In-plane XRD patterns. The incident angle is ω = 0.4°, and the scattering vector is along the [100] of Mn_4N films. The insets show the RHEED images of the Mn_4N layers along the [100] direction of each substrate. Arrows indicate the superlattice diffractions from N atoms at the body-centered site. (e, f) ω-scan rocking curves for Mn_4N films on MgO(001) and STO(001), respectively. (g, h) TEM cross sections of Mn_4N films on MgO(001)[41] (Copyright 2014 AIP Publishing) and STO(001).[16] Copyright 2019 American Chemical Society.

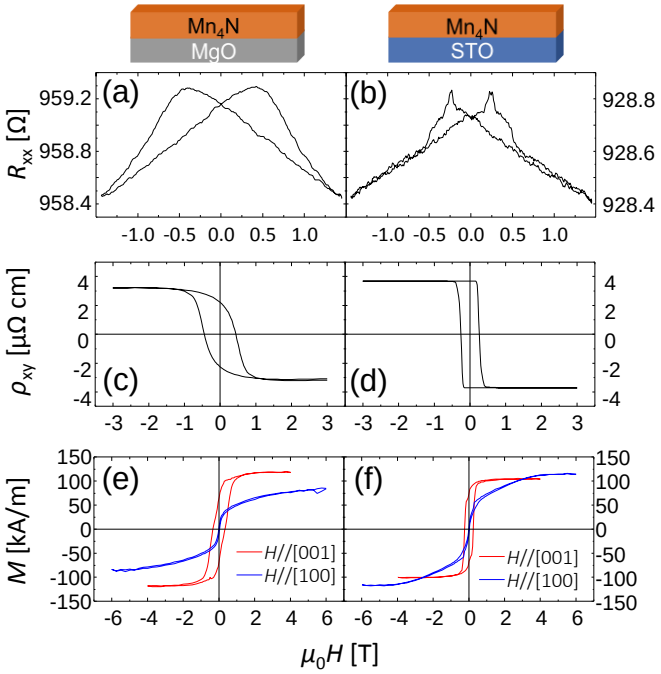

Fig. 3 (a, b) Longitudinal resistance against magnetic field normal to the plane. (c, d) Anomalous Hall effect hysteresis loops. (e)(f) Out-of-plane hysteresis loops measured by VSM. (a, c, e) correspond to the Mn_4N films on MgO(001), and (b, d, f) to the Mn_4N films on STO(001).[58)] Copyright 2018 Japan Society of Applied Physics.

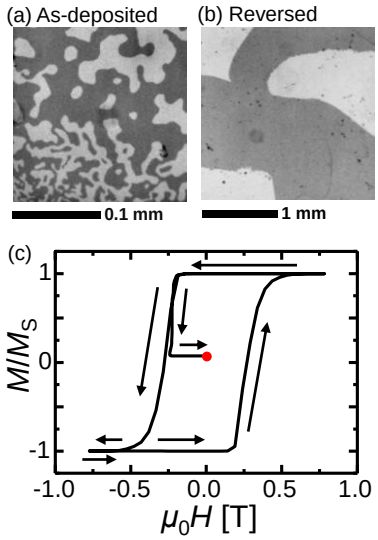

Fig. 4 (a) MOKE image of the Mn_4N films on STO(001) in the as-deposited state. (b) MOKE image of the sample after the partial reversal of fig. (c). (c) Magnetization curve illustrating the partial reversal process, monitored by anomalous Hall effect in the sample. The red dot corresponds to the final magnetization state, used for (b).[58)] Copyright 2018 Japan Society of Applied Physics.

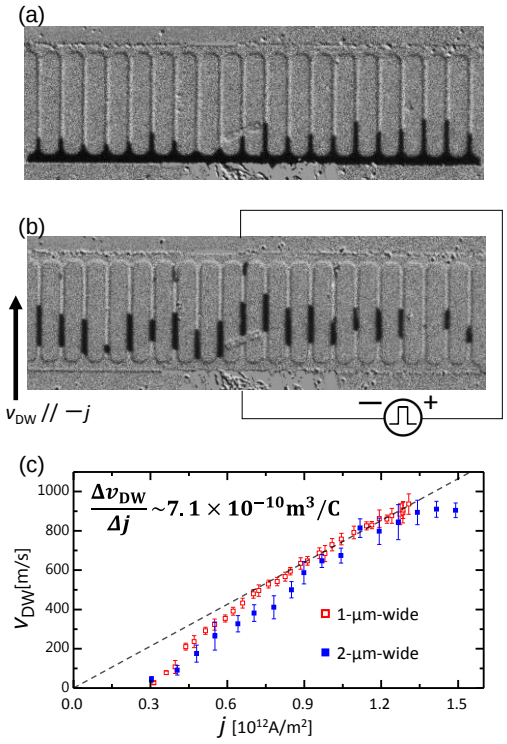

Fig. 5 (a) Differential MOKE image after domain nucleation using a field pulse of 0.6 T. (b) Differential MOKE image after several 1 ns current pulses. The area through which the DW propagated appears in black. The DW motion direction is opposite to the current, and thus follows the electrons flow.[16] (c) Current density dependence of v_{DW} measured at RT. Both the 1 and 2-μm-wide strips possess similar behaviors.[16] The DW mobility is calculated to be 7.1 × 10^{-10} m^3 C^{-1}. Copyright 2019 American Chemical Society.

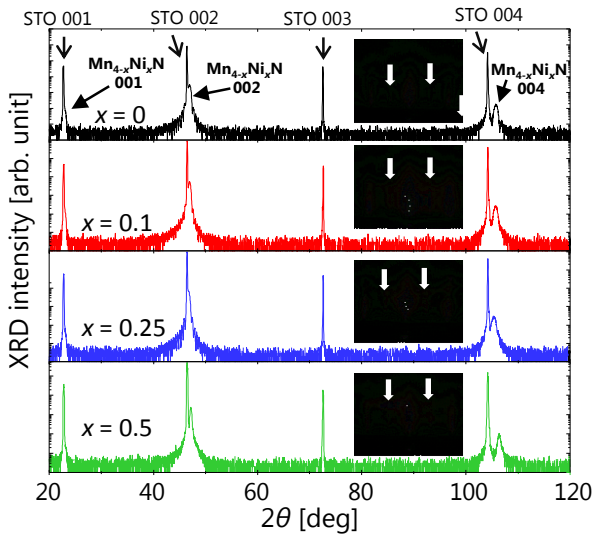

Fig. 6 Out-of-plane XRD profiles of $Mn_{4-x}Ni_xN$ (x = 0, 0.1, 0.25, 0.5) films on STO(001).[20] The insets show the RHEED patterns taken along the [100] azimuth. The arrows show superlattice diffractions from N atoms at the body-centered sites. Copyright 2019 AIP Publishing.

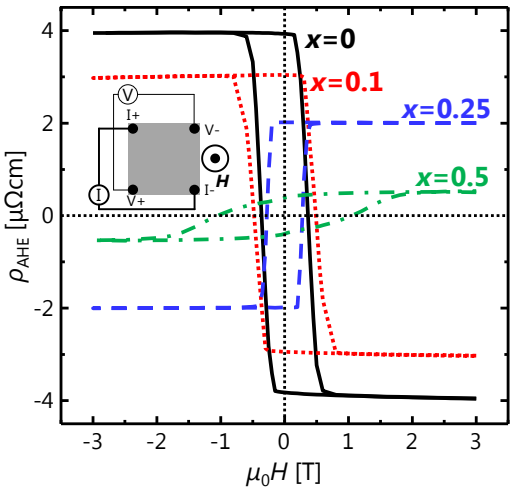

Fig. 7 Dependence of the Hall resistivity ρ_{AHE} on a perpendicular magnetic field for $Mn_{4-x}Ni_xN$ (x = 0, 0.1, 0.25, 0.5) films on STO(001) at RT.

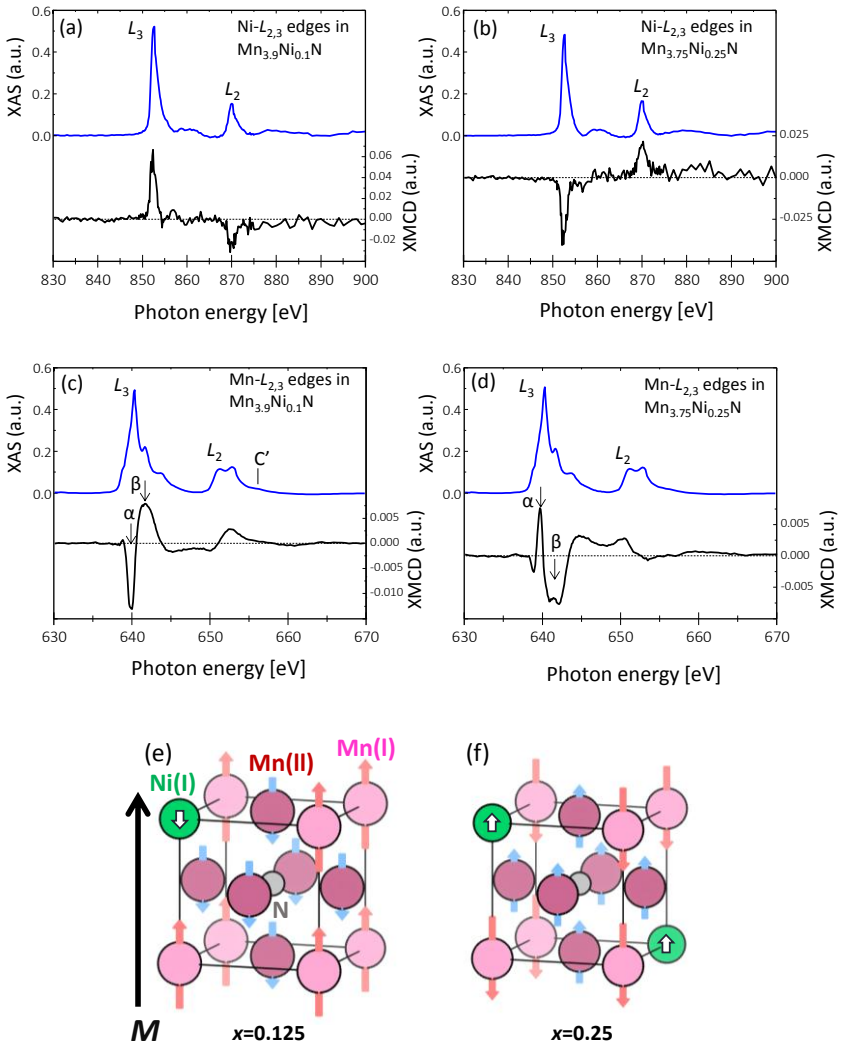

Fig. 8 XAS (blue) and XMCD (black) spectra in (a, c) $Mn_{3.9}Ni_{0.1}N$ films and (b, d) $Mn_{3.75}Ni_{0.25}N$ films at (a, b) Ni-$L_{2,3}$ edges and (c, d) Mn-$L_{2,3}$ edges.[21] The sharp peak (α) and broad peak (β) in (c, d) originate mainly from Mn(I) and Mn(II), respectively. The reversal of the XMCD signals between (a) and (b) and between (c) and (d) means that the direction of magnetic moments of Mn and Ni is reversed between them.

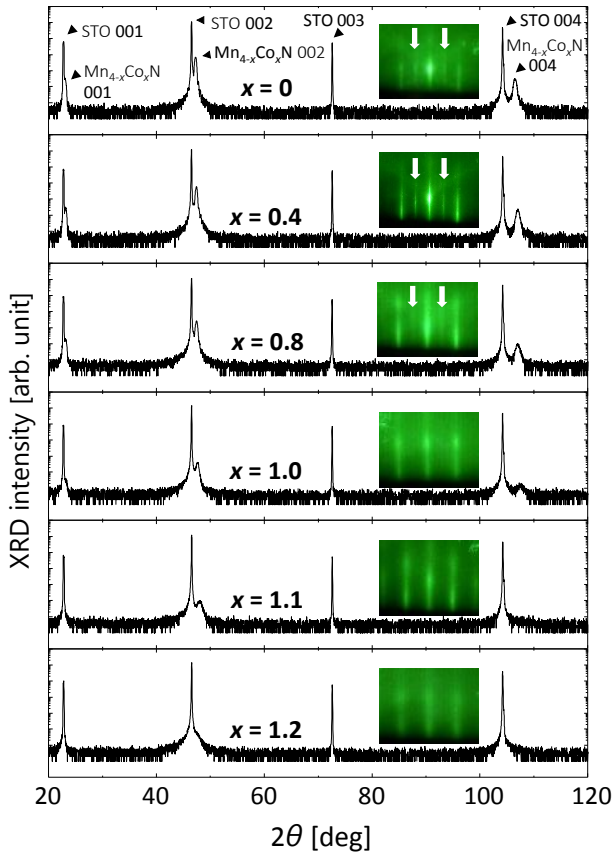

Fig. 9 Out-of-plane XRD profiles of $Mn_{4-x}Co_xN$ (x = 0, 0.4, 0.8, 1.0, 1.1, 1.2) films on STO(001).[23] The insets show the RHEED patterns taken along the [100] azimuth. The arrows indicate the superlattice diffractions from N atoms at the body-centered site. Copyright 2020 American Physical Society.

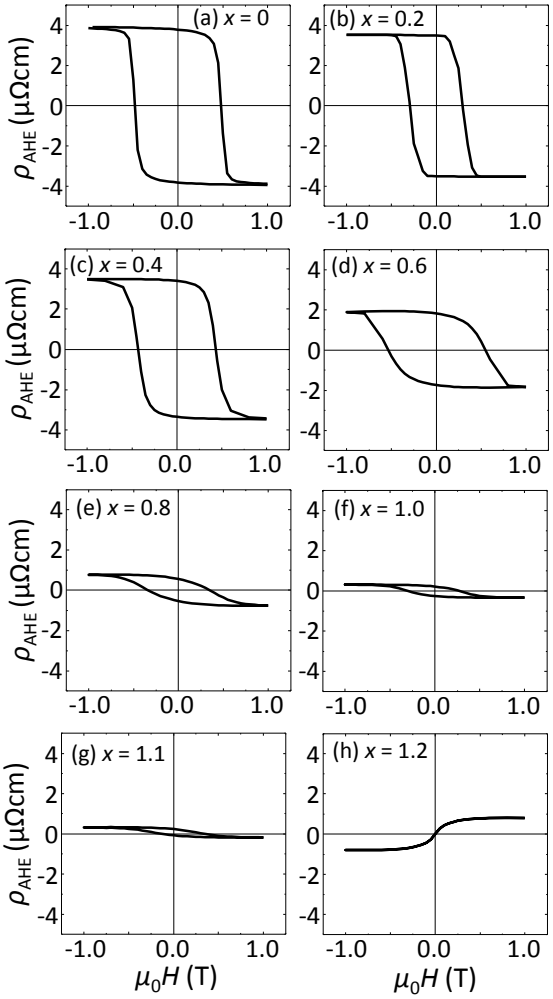
(a) x = 0
(b) x = 0.2
(c) x = 0.4
(d) x = 0.6
(e) x = 0.8
(f) x = 1.0
(g) x = 1.1
(h) x = 1.2
ρAHE (μΩcm)
μ0H (T)
4
2
0
-2
-4
-1.0
0.0
1.0

Fig. 10 Dependence of the anomalous Hall resistivity ρ_{AHE} on the perpendicular magnetic field for $Mn_{4-x}Co_xN$ (x = 0, 0.2, 0.4, 0.6, 0.8, 1.0, 1.1, 1.2) films on STO(001) at RT.[23)]

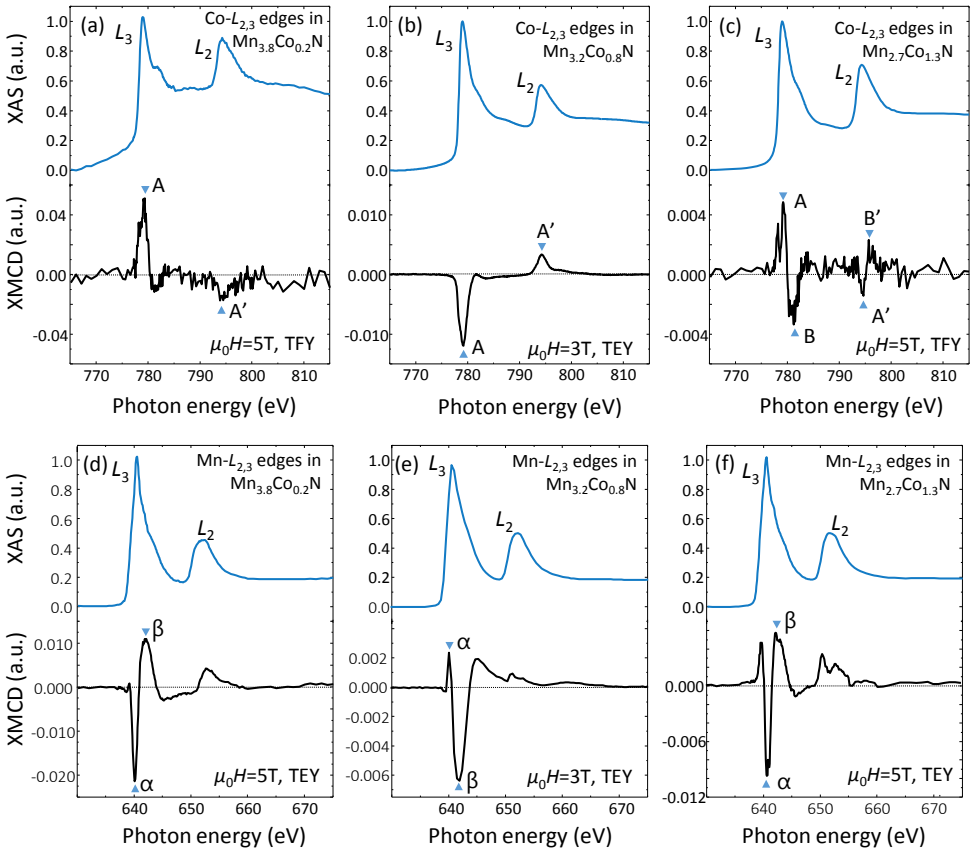
(a) Co-$L_{2,3}$ edges in $Mn_{3.8}Co_{0.2}N$
(b) Co-$L_{2,3}$ edges in $Mn_{3.2}Co_{0.8}N$
(c) Co-$L_{2,3}$ edges in $Mn_{2.7}Co_{1.3}N$
(d) Mn-$L_{2,3}$ edges in $Mn_{3.8}Co_{0.2}N$
(e) Mn-$L_{2,3}$ edges in $Mn_{3.2}Co_{0.8}N$
(f) Mn-$L_{2,3}$ edges in $Mn_{2.7}Co_{1.3}N$
XAS (a.u.)
XMCD (a.u.)
Photon energy (eV)
μ_0H=5T, TFY
μ_0H=3T, TEY
μ_0H=5T, TEY

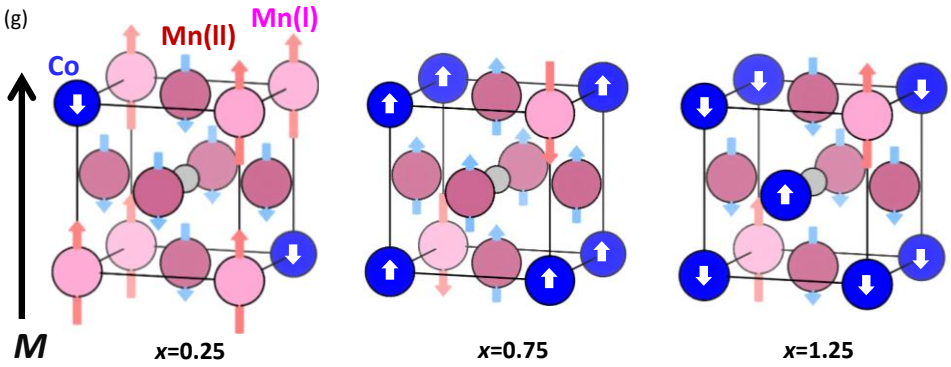
(g)
Co
Mn(II)
Mn(I)
M
x=0.25
x=0.75
x=1.25

Fig. 11 XAS (blue) and XMCD (black) spectra in (a, d) $Mn_{3.8}Co_{0.2}N$ films, (b, e) $Mn_{3.2}Co_{0.8}N$ films, and (c, f) $Mn_{2.7}Co_{1.3}N$ films at (a, b, c) Co-$L_{2,3}$ edges and (d, e, f) Mn-$L_{2,3}$ edges.[23] The sharp peak (α) and broad peak (β) in (d, e, f) originate mainly from Mn(I) and Mn(II), respectively. The reversal of the XMCD signals between (a) and (b) and between (d) and (e) means that the direction of magnetic moments of Mn and Co is reversed between them. In (c), the sign of the XMCD signal of Co(I) (A–A') reverses again and another signal with the opposite sign (B–B') of Co(II), appears, meaning that the magnetic moment of Co(II) is antiparallel to that of Co(I).